Hindawi
Geofluids
Volume 2020, Article ID 4578967, 16 pages
https://doi.org/10.1155/2020/4578967

Research Article

Hydrochemical Characteristics and Evolution Mode of Cold Seeps in the Qiongdongnan Basin, South China Sea

Zhifeng Wan,[1] Chongmin Chen,[1] Jinqiang Liang,[2] Wei Zhang,[2] Wei Huang,[2] and Pibo Su[2]

[1]*School of Marine Sciences, Sun Yat-Sen University/Southern Marine Science and Engineering Guangdong Laboratory (Zhuhai), Zhuhai 519000, China*
[2]*MLR Key Laboratory of Marine Mineral Resources, Guangzhou Marine Geological Survey, Ministry of Natural Resources, Guangzhou 510075, China*

Correspondence should be addressed to Jinqiang Liang; ljinqiang@hydz.cn and Wei Zhang; zwgmgs@foxmail.com

Received 26 July 2019; Revised 8 October 2019; Accepted 29 October 2019; Published 7 January 2020

Academic Editor: Paolo Fulignati

Submarine cold seeps have recently attracted significant attention and are among the most effective indicators of gas hydrate in the oceans. In this study, remotely operated vehicle (ROV) observations, seismic profiles, core sediments, bottom seawater, and fluid vented from cold seeps in the deep-water Qiongdongnan Basin were used to investigate the origin and evolution of cold seeps and their relationships with gas hydrate. At stations A, B, and C, inactive cold seeps with dead clams, cold seep leakage with live clams, and active cold seeps with a rich mussel presence, respectively, were observed. The salinity and Na^+ and Cl^- concentrations of the cold seeps were different from those of typical seawater owing to gas hydrate formation and decomposition and fluid originating from various depths. The main ion concentrations of the bottom seawater at stations B and C were higher than those at station A, indicating the substantial effects of low-salinity cold seep fluids from gas hydrate decomposition. The Na^+-Cl^-, K^+-Cl^-, Mg^{2+}-Cl^-, and Ca^{2+}-Cl^- diagrams and rare earth element distribution curves of the water samples were strongly affected by seawater. The concentrations of trace elements and their ratios to Cl^- in the bottom seawater were high at the stations with cold seeps, suggesting the mixing of other fluids rich in those elements. Biochemical reactions may also have caused the chemical anomalies. Samples of HM-ROV-1 indicated a greater effect of upward cold seep fluids with higher B/Cl^-, Sr/Cl^-, and Ba/Cl^- values. Moreover, the Re/Cl^- value varied between fluid vents, possibly due to differences in Re precipitation strength. Differences in cold seep intensity are also believed to occur between areas. The cold seep fluxes changed from large to small before finally disappearing, showing a close connection with gas hydrate formation and decomposition, and influenced the local topography and ecosystems.

1. Introduction

A cold seep is a natural fluid spillage phenomenon in which fluid, usually rich in hydrothion and hydrocarbons, is discharged from submarine sediments and transported under the influence of a pressure gradient [1]. Generally related to the decomposition of gas hydrate [2] or the upward migration of gas and oil beneath the seafloor along geologically weak zones, cold seeps are widely distributed around the world and play an indicative role in the exploration of deep-water oil and gas resources [3]. Furthermore, gas hydrate is a significant gas source at cold seeps, and the cold seep fluid flow velocity can also affect the hydrate formation rate [4, 5]. Cold seeps are among the most effective indicators in explorations for gas hydrate in the ocean [3].

Cold seeps are usually characterized by the migration and seepage of methane-rich fluids. Owing to their special fluid environment and unique ecosystem, these seeps experience complex and diverse biochemical reactions. The coupling of

sulfate reduction and the anaerobic oxidation of methane (AOM) is a vital biochemical reaction [6]:

$$CH_4 + SO_4^{2-} \longrightarrow HCO_3^- + HS^- + H_2O. \quad (1)$$

AOM increases the alkalinity of the surrounding fluid, leading to local oversaturation of bicarbonate produced by methane and enhancement of carbonate precipitation.

Several additional reactions such as organoclastic sulfate reduction (OSR) [7], authigenic precipitation of certain metallic elements [8], or formation and decomposition of gas hydrate [9] may also result in abnormal phenomena in the surrounding seawater, sediments, and ecosystems.

Cold seep fluids include the pore water left in sediments and leakage into the overlying seawater. The chemical anomalies of bottom seawater comprehensively represent the source and composition of cold seep fluid as well as the biochemical reaction and interaction occurring between the water and the surrounding rock during fluid migration. In recent years, detailed geochemical analyses of cold seeps were performed internationally on columnar sediments and pore water samples obtained through ocean drilling and submarine observation [10–14]. Such research has led to better understanding of the characteristics of pore water in cold seeps and the relationship between cold seeps and gas hydrates [15, 16]. The geochemical anomaly of pore water is considered to be an important indicator of the existence of gas hydrates [17, 18]. Previous studies have indicated that the formation and decomposition of gas hydrate changes the concentrations of Cl^-, Ca^{2+}, Mg^{2+}, SO_4^{2-}, and Sr and the Mg^{2+}/Ca^{2+}, Sr/Ca^{2+}, and Sr/Cl^- ratios in interstitial water. The values of some isotopes such as $\delta^{18}O$, δD, and δ^7Li also show anomalies [19–24]. During upward migration, the seepage fluid in the cold seep mixes pore water from different strata and finally vents into the bottom seawater, intensively affecting the chemical characteristics of the bottom seawater. In addition, due to the significant exchange of matter between the bottom seawater and pore water in the bottom shallow surface sediments, the formation and decomposition of gas hydrate in the bottom shallow surface sediments will be influenced by the bottom seawater, and the anomalies resulting from gas hydrate can also be reflected in the bottom seawater to some extent. Compared with pore water, which is of more general significance in chemical exploration of hydrate fluid, although the sampling of bottom seawater is simpler, relatively few studies have been conducted on cold seep bottom seawater. Most of those studies have been focused on the indicator function of bottom seawater in relation to gas hydrate [22, 24]. It has been found that seawater at the bottom of a cold seep area often has a high methane content and that the total dissolved CO_2 concentration increases owing to local oxidation of the methane overflow [25]. In addition, the isotopic information of the bottom seawater indicates abnormalities such as low $\delta^{13}C$ and high δ^4He [26–28]. However, most investigations of the origin and evolution of cold seeps have only been based on combinations of the chemical anomalies of shallow bottom seawater, and submarine seismic profile information in the absence of drilling information remains insufficient, impeding further understanding of the relationship between cold seep activities and the accumulation of gas hydrates.

Generally, the components and intensity of fluid in cold seeps vary in time and space. The Qiongdongnan Basin (QDNB) is a key area for investigating cold seeps and gas hydrates in the northern slope of the South China Sea (SCS) [29–32]. Recent investigations have been performed on the cold seep systems in the QDNB, including gas bubble plumes, seafloor features, near-seafloor gas hydrates, and the fluid flow structure by using multibean data, sediment cores, multichannel seismic data, and other resources [33, 34]. However, there remains a lack of comprehensive analysis of the evolution characteristics of cold seep activities and the relationship between cold seeps and the formation and decomposition of gas hydrates based on combined shallow biochemical information and deep structural data (especially seismic profile data) in this region.

This article consists of 6 sections. Section 2 clearly described the study area, QDNB. Section 3 presented the seafloor observations at various stations, the acquisition of samples and seismic data, and chemical and analytical procedures. The study results of section 3 were displayed in section 4. Section 5 analyzed and compared the geochemical characteristics of samples of bottom seawater and fluid vented from cold seeps at various locations in the cold seep area of the deep-water QDNB. Besides, the results were combined with high-precision seismic data to reveal the relationships between the cold seep conditions and chemical anomalies of the bottom seawater obtained from the different locations in this section, realizing the purpose of combining the shallow phenomena with deep structure analysis to determine the formation and development mechanism of cold seeps in the deep-water area of the QDNB and their spatiotemporal coupling relationship with the formation and decomposition of gas hydrate. Section 6 concisely summarized the main conclusions of our research, and we believed that the formation and evolution of cold seeps require further research.

2. Regional Setting

The QDNB, a large NE-trending Cenozoic sedimentary basin, lies in the western section of the continental slope in the northern SCS, with Hainan Island to the north, Yinggehai Basin to the west, and the Pearl River Mouth Basin to the east. The QDNB covers an area of about $8.3 \times 10^4\,km^2$ with ~60% of the area in deep-water settings.

The tectonic evolution of the QDNB can be divided into two stages: the Eocene-Oligocene rift stage and the Neogene post-rift thermal subsidence stage [35]. After the rift stage, a series of half-grabens or depressions set southward are filled with lacustrine sediments [29]. Since the Miocene, the QDNB has deposited thick marine sediments dominated by sedimentary mudstone following the Neogene thermal subsidence stage, with a maximum deposition thickness of more than 8 km and a maximum burial depth of more than 9.4 km. The maximum thickness of the Cenozoic sediments in the basin is 12 km, and the maximum area of hydrocarbon

generation depression is more than 9000 km^2. In addition, overpressure in the basin is common owing to the rapid deposition of terrestrial sediments and the pressurization of hydrocarbon generation. Currently, the Tibet Plateau shows strong uplift, which has caused the sediment supply from the Red River to increase dramatically. Therefore, strong sedimentary continental slope deposition occurs in the QDNB, with a maximum sedimentation rate of 1.2 mm per year [36] and a geothermal gradient of 39–45°C/km [37]. The QDNB is presently in the stage of particularly strong sediment accumulation [34]. The Neogene sedimentary strata in the basin are rich in organic matter, which provides a gas source foundation for the generation of abundant oil and gas, and the emergence of fluid activity.

The QDNB is characterized by complex and diverse structures, including abundant fault depression, uplift and low uplift, and submarine channels. Pathways such as polygonal faults [38], mud diapirs, gas chimneys, and associated faults have been discovered in the QDNB [39, 40], all of which are beneficial for fluid migration. Additionally, past intense magmatic activity occurring in the northern margin of the SCS may also have controlled the evolution of the QDNB and the formation and migration of the fluids [41, 42].

To summarize, the combination of a thick sedimentary sequence and high geothermal gradient, as well as the transport and overpressure functions of gas chimneys or diapirs, provides favorable conditions for the formation and migration of natural gas in the QDNB and the development of active cold seeps [38].

3. Materials and Methods

3.1. Seafloor Observations and Sampling. The seafloor observation images and experimental samples used in this study were acquired by the Guangzhou Marine Geological Survey in 2018 during station sampling in the deep-water area of the QDNB using the remotely operated vehicle (ROV) *Haima* carried by the Chinese vessel *Haiyang-6*. As the sampling method of this voyage, the ROV observation dive used mechanical arms to collect samples such as sediments, submarine organisms, and carbonates. Conductivity, temperature, and depth (CTD) sensors and pressure-holding water intake devices were also used to sample the bottom seawater. The specific locations of this investigation were stations A, B, and C in Figure 1, and vents HM-ROV-1 and HM-ROV-2 were located at station C. At station A, the cold seep was no longer active, and numerous large dead clams were found (Figure 2(a)). At station B, cold seep leakage was present, as well as numerous large live clams. At station C, fluid of active cold seep flow was present, as were many relatively small mussels (Figures 2(c)–2(e)). In addition, the plume of HM-ROV-1 flowed continually (Figure 2(b)), and a small mud dome was discovered near the vent. Gas hydrate was clearly detected at HM-ROV-1 during this sampling (Figure 3). Mussels were distributed mainly at the bottom of the mud dome. Moreover, a submarine dome and numerous mussels were found near HM-ROV-2.

The samples used in this study included the bottom seawater collected from each station and vent fluids from HM-ROV-1 and HM-ROV-2 at station C.

The seismic profiles employed in the study were collected by the Guangzhou Marine Geological Survey from 2007 to 2013. We selected mainly seismic lines that extended through several vents and paleovents in the cold seep region to study possible fluid migration pathways and their connections with the seafloor.

3.2. Chemical and Analytical Procedures. The main ion, trace element, and rare earth element (REE) concentrations were measured after the water samples were filtered through a 0.22 μm membrane.

The SO_4^{2-}, Cl^-, Ca^{2+}, and Na^+ concentrations were determined by using a Dionex ICS-5000+ ion chromatograph with an analytical precision of <5% at the South China Sea Institute of Oceanology, Chinese Academy of Sciences. The anions (SO_4^{2-} and Cl^-) and cations (Ca^{2+} and Na^+) were determined by 500-fold and 100-fold dilution, respectively, using ultrapure water. In the anion concentration analyses, 28 mM KOH was used as the eluent, and an IonPac AS11HC analytical column was used for ion separation. For the cation concentration analyses, methanesulfonic acid (20 mM) was the eluent, and an IonPac CS12A analytical column was used for ion separation.

Both the trace elements and REEs of our samples were measured by ALS Chemex (Guangzhou) Co. Ltd. using test method number LU-MS02. After solution acidification, precipitation and ion exchange chromatography were used to enrich and separate the elements. The REEs were then tested via fan-shaped magnetic field ionization mass spectrometry (HR-ICP-SFMS) (see [43] for detailed operating procedures).

After receiving the experimental data, we calculated the ratios of the main ions—including Na^+, Ca^{2+}, K^+, Mg^{2+}, and SO_4^{2-}—to Cl^- (Table 1) and also calculated the ratios of several trace elements, such as B, Sr, and Ba, to Cl^- (Table 2). In addition, we generated comparison images of the main cations—including Na^+, Ca^{2+}, K^+, and Mg^{2+}—to Cl^- and did the same for some trace elements, including B, Sr, Ba, and Re (Figures 4 and 5). Moreover, to define the REE sources in bottom seawater and vent fluids further, we standardized the REE values in the water samples based on Post-Archean Australian Shale (PAAS), created an REE distribution curve (Figure 6), and calculated the Eu and Ce anomalies. In this study, the Eu and Ce anomalies were defined as follows [44]:

$$\delta\mathrm{Ce} = \frac{2\mathrm{Ce}_N}{\mathrm{La}_N + \mathrm{Pr}_N}, \tag{2}$$

$$\delta\mathrm{Eu} = \frac{2\mathrm{Eu}_N}{\mathrm{Sm}_N + \mathrm{Gd}_N}, \tag{3}$$

where Ce_N, La_N, Pr_N, Eu_N, Sm_N, and Gd_N represent the values of Ce, La, Pr, Eu, Sm, and Gd normalized by PAAS [45], respectively. $\delta Ce > 1$ indicates a positive Ce anomaly; otherwise, the Ce anomaly is negative. Similarly, $\delta Eu > 1$ and $\delta Eu < 1$ indicate positive and negative Eu anomalies, respectively.

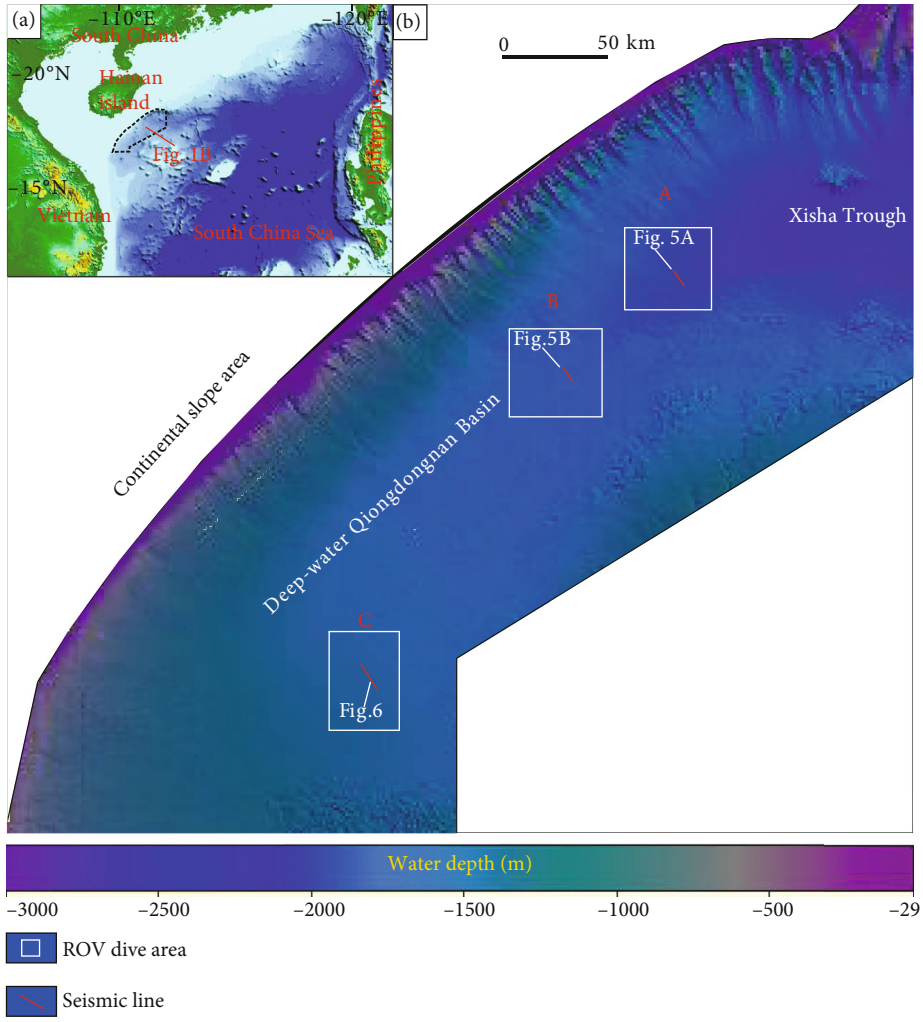

Figure 1: (a) Map of the study area in the Qiongdongnan Basin (QDNB), northern South China Sea (SCS). The QDNB lies in the western section of the continental slope in the northern SCS, with Hainan Island to the north. (b) Positions of stations A, B, and C. The white boxes represent ROV dive areas in this research. The red lines represent the seismic lines that were selected and used. The seismic line at station A extends through an inactive seep site, while those at stations B and C extend through modern cold seeps. Two evidently active cold-seep vents, HM-ROV-1 and HM-ROV-2, were located at station C.

4. Results

4.1. Main Ions. The cations in the samples mainly included Na^+, Mg^{2+}, Ca^{2+}, and K^+, whereas the anions were dominantly Cl^- and SO_4^{2-}, where $Na^+ > Mg^{2+} > K^+ > Ca^{2+}$ and $Cl^- > SO_4^{2-}$. Furthermore, the concentrations of Na^+ and Cl^- showed the largest proportions (Tables 3 and 4).

The concentrations of Na^+, Mg^{2+}, Ca^{2+}, K^+, Cl^-, and SO_4^{2-} in the bottom seawater samples were lower than those of typical seawater ions. The concentrations of these ions in the bottom seawater from stations C and B were similar and lower than those at station A.

The concentrations of Na^+, Mg^{2+}, Ca^{2+}, K^+, Cl^-, and SO_4^{2-} at HM-ROV-1 were similar to those in the bottom seawater samples from station C, with relatively low concentrations compared to those of typical seawater ions and about half of those at HM-ROV-2. The concentrations of these ions at HM-ROV-2 and in typical seawater were similar, and the Cl^- concentration was slightly higher than that in typical seawater (Tables 3 and 4).

4.2. Trace Elements

4.2.1. B and Sr. The trends of the concentrations of the B and Sr of the bottom seawater were similar at each station, with the lowest concentrations at station A. In the other areas, the concentration of B was 4.6–4.9 mg/L (Table 2), which was higher than the average concentration of B in typical seawater (4.5 mg/L; Figure 5). The Sr/Cl^- and B/Cl^- values at station A were similar to those of seawater, typically at 0.396–0.406‰ and 0.232–0.236‰, respectively. The values at stations B and C were higher, about twice those of seawater.

The concentrations of B and Sr at HM-ROV-1 were lower than those at HM-ROV-2 (Table 2, Figure 5). The

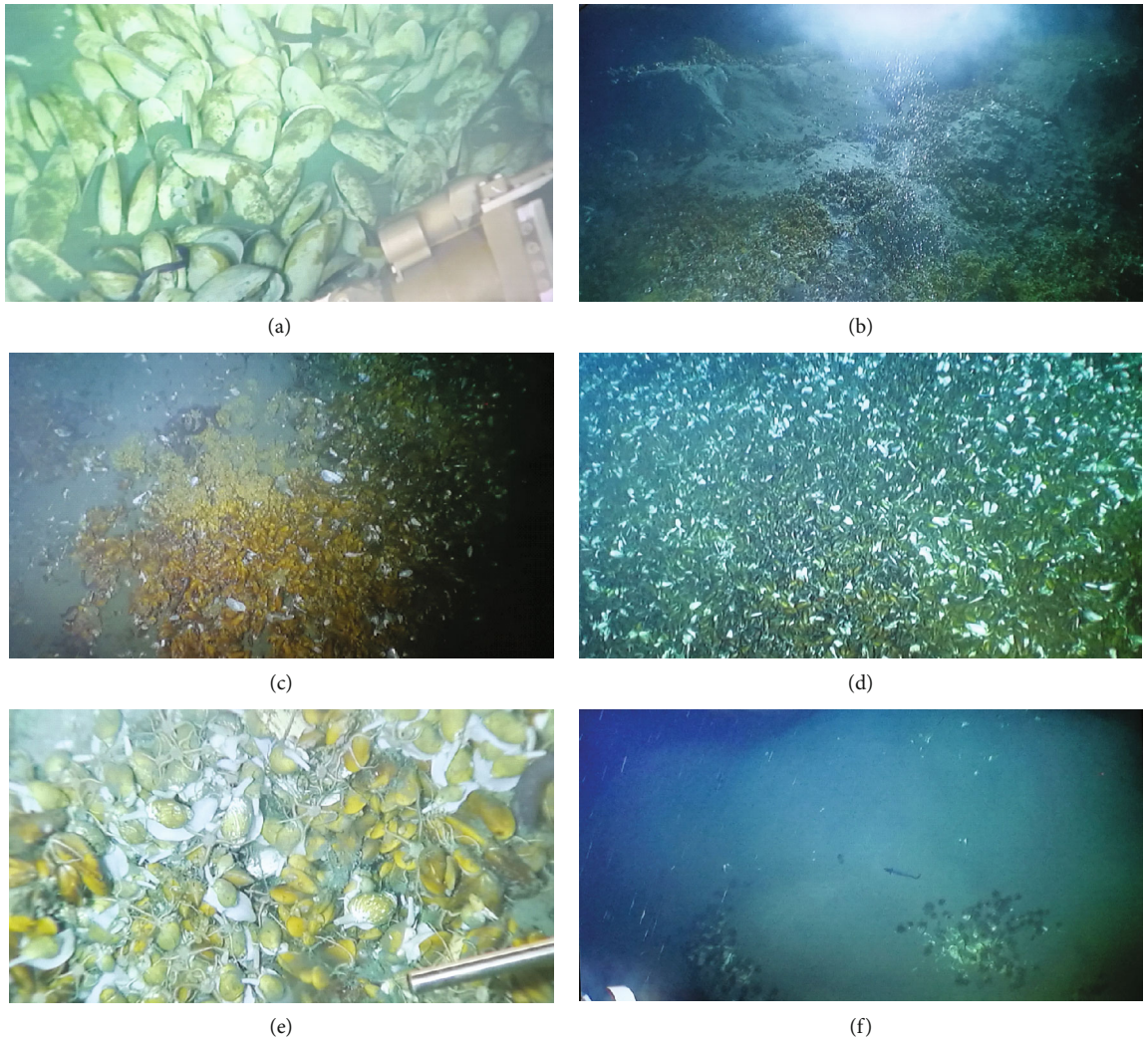

Figure 2: Seafloor observations at different stations taken by ROV: (a) dead clams at station A, (b) continually flowing plume in HM-ROV-1, (c) numerous mussels around HM-ROV-1, (d and e) abundant mussels around HM-ROV-2, (f) submarine mud dome near HM-ROV-2.

Figure 3: Sampling near HM-ROV-1. Some of the bright spots in the image are bubbles of gas hydrate.

Sr/Cl^- and B/Cl^- ratios at HM-ROV-2 were similar to those of seawater, as were nearly half those at HM-ROV-1 (Table 2).

4.2.2. Ba. The average concentration of Ba at the different stations was higher than that in typical seawater, at 14 μg/kg, as was the ratio Ba/Cl^- (Figure 5).

The concentration of Ba in the bottom seawater decreased in the order C > B > A and C ≈ 2A, and the ratio Ba/Cl^- followed the same order (Figure 5).

Table 1: Ratios of Na^+/Cl^-, K^+/Cl^-, Mg^{2+}/Cl^-, and Ca^{2+}/Cl^- at different stations.

Site	Na^+/Cl^-	$Mg2^+/Cl^-$	Ca^{2+}/Cl^-	K^+/Cl^-	SO_4^{2-}/Cl^-
HM-ROV-1	0.81	0.082	0.017	0.020	0.044
HM-ROV-2	0.77	0.092	0.017	0.017	0.046
Station A	0.81	0.083	0.017	0.017	0.051
Station B	0.79	0.086	0.017	0.021	0.037
Station C	0.79	0.091	0.017	0.021	0.039

The concentration of Ba at HM-ROV-1, which was similar to that in the bottom seawater at station C, was about half of that at HM-ROV-2. The Ba/Cl^- ratio at HM-ROV-2 was slightly lower than that at HM-ROV-1 (Table 2).

4.2.3. Re. The concentration of Re in the bottom seawater at stations B and C was lower than that at station A, and the concentration of Re at station A was similar to the average

Table 2: Concentrations of B, Sr, Ba, and Re and ratios B/Cl^-, Sr/Cl^-, and Re/Cl^-.

Sample	B (μg/L)	B/Cl^-	Sr (μg/L)	Sr/Cl^-	Ba (μg/L)	$Ba/Cl^-(10^{-6})$	Re (μg/L)	Re/Cl^- (10^{-10})
HM-ROV-1								
CM-1	3760	0.00042	6178	0.00069	15	1.7	0.0068	7.6
CM-2	3851	0.00043	6383	0.00071	15	1.7	0.0061	6.8
Average	3806	0.00043	6281	0.00070	15	1.7	0.0065	7.2
HM-ROV-2								
CM-3	4702	0.00023	8024	0.00039	31	1.5	0.0079	3.9
CM-4	4785	0.00023	7947	0.00039	31	1.5	0.0060	2.9
Average	4744	0.00023	7986	0.00039	31	1.5	0.0070	3.4
Station A								
CM-5	2980	0.00020	5199	0.00035	13	0.88	0.0054	3.7
CM-6	4007	0.00027	6776	0.00046	17	1.2	0.0076	5.2
Average	3494	0.00024	5988	0.00041	15	1.0	0.0065	4.4
Station B								
CM-7	4818	0.00045	8357	0.00079	24	2.3	0.0075	7.1
CM-8	4789	0.00045	8202	0.00077	24	2.3	0.0097	9.1
Average	4804	0.00045	8280	0.00078	24	2.3	0.0086	8.1
Station C								
CM-9	4663	0.00049	8111	0.00085	29	3.1	0.0081	8.5
CM-10	4705	0.00049	8108	0.00085	31	3.2	0.0077	8.0
Average	4684	0.00049	8110	0.00085	30	3.1	0.0079	8.2

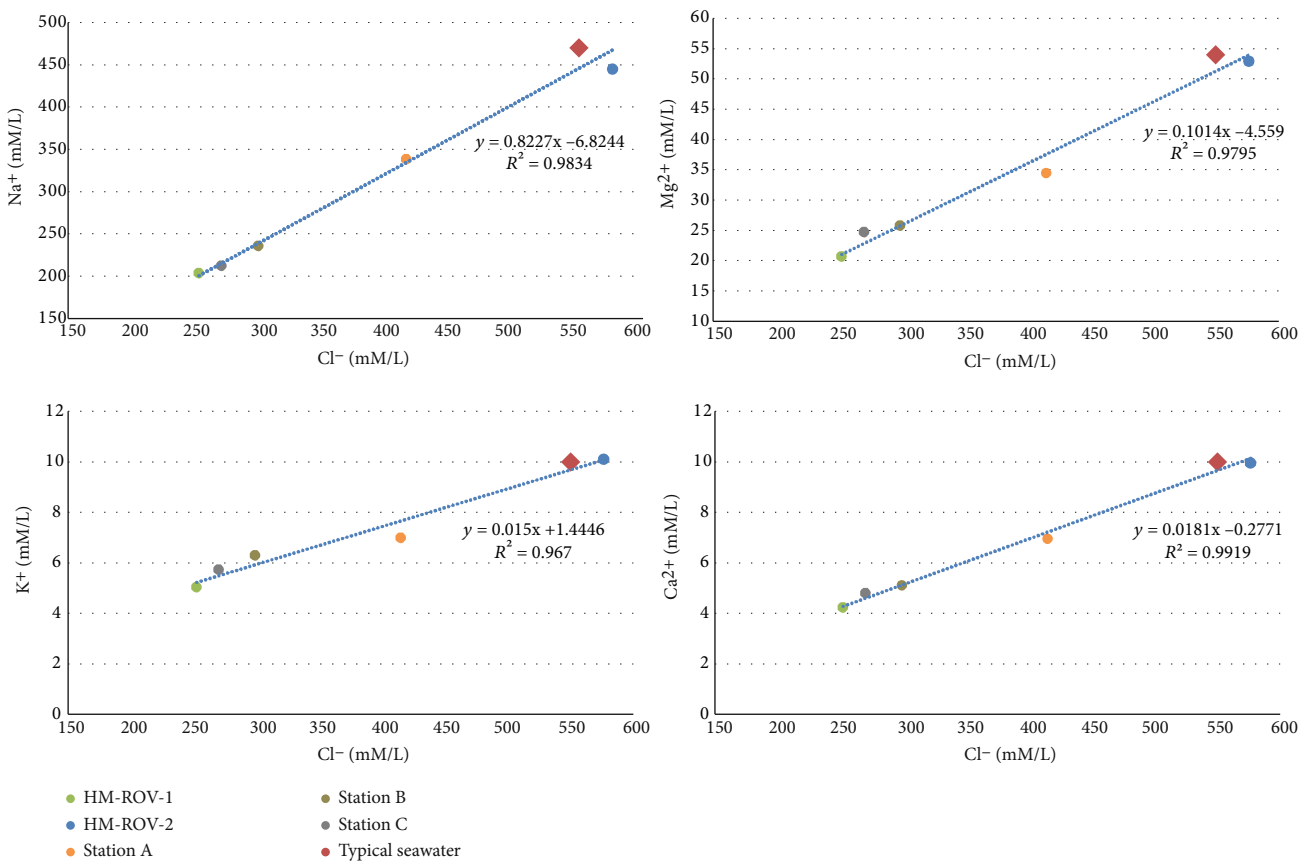

Figure 4: Comparison of the concentrations of Na^+, Mg^{2+}, K^+, and Ca^{2+} with the Cl^- concentration, separately. The values from our samples and those of typical seawater lie roughly along a straight line, proving the strong influence of seawater and similar sources.

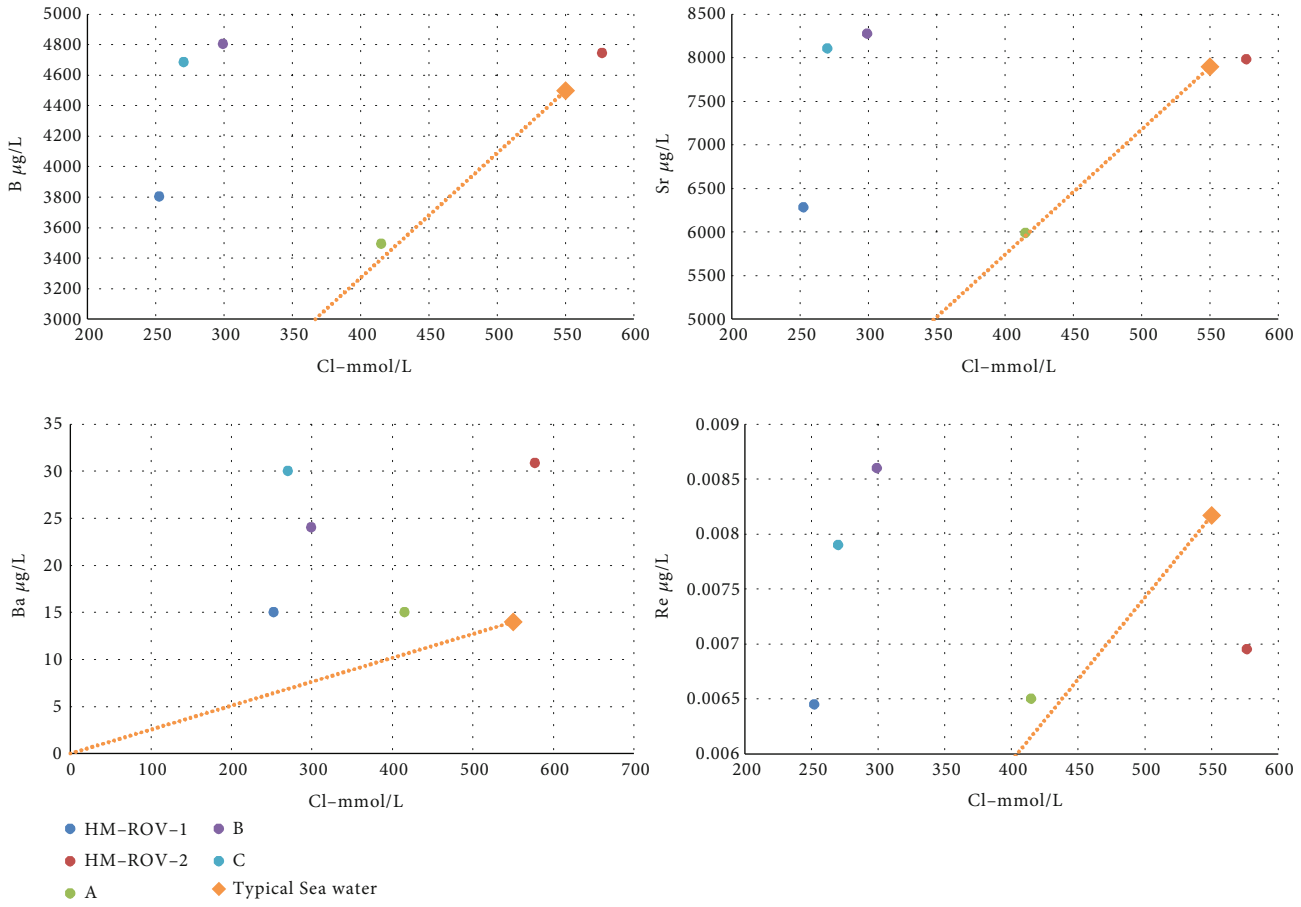

Figure 5: Comparison of the concentrations of B, Sr, Ba, and Re with the Cl^- concentration, separately. The dotted line represents the connection between the typical seawater point and the point (0, 0).

concentration of Re in the Pacific Ocean, at 43.9 ± 0.3 pmol /kg [46] (Figure 5). Moreover, the ratio Re/Cl^- at stations B and C was higher than that in the Pacific Ocean, and the value at station A was similar.

The ratio Re/Cl^- at HM-ROV-2 and HM-ROV-1 was lower and higher, respectively, than that in the Pacific Ocean (Table 2).

4.3. Rare Earth Elements REE. All of the samples had low REE concentrations, showing different degrees of negative Ce anomalies. δCe increased in the order A < B < HM-ROV-1 < C < HM-ROV-2. The results at station B and HM-ROV-1 showed no Eu anomalies; station A showed a slightly negative Eu anomaly; and positive Eu anomalies were found at station C and HM-ROV-2 (Table 5).

5. Discussion

5.1. Geochemical Anomalies of Cold Seep in the QDNB

5.1.1. Differences in Main and Trace Elements under the Influence of Cold Seep. The origin and evolution of cold seeps are mainly related to seawater, sediment alteration, clay dehydration, organic degradation, and the formation and decomposition of shallow gas hydrates [46]. Some researchers have determined that the formation of the cold seep in the southwestern QDNB is closely related to the gas hydrate decomposition [9]. The decomposition of gas hydrate releases fresh water, thereby reducing the salinity and concentrations of Cl^- and Na^-, among other ions. In addition, we consider the upward migration of fluid from the deep strata of the QDNB to be a significant factor affecting the chemical composition of cold seeps as some of the numerous faults and gas chimneys acting as the migration pathways are characterized by strings of "beads" indicating the migration of low-velocity fluid [47, 48] (Figure 7). The QDNB experienced the alternation of continental and marine facies during the Neogene, leaving different marine or lacustrine sediments among the strata [29]. Sedimentary pore water from different periods can reflect the salinity of the sedimentary water environment at that time, which had various effects on cold seeps.

Although most of the concentrations of Na^+, Mg^{2+}, Ca^{2+}, K^+, Cl^-, and SO_4^{2-} in our samples were lower than those of typical seawater, no Na^+ enrichment or K^+ deficit was apparent. Thus, the clay mineral dehydration was not significant enough, and the decomposition of gas hydrate or the upward migration of low-salinity groundwater may be main factors affecting the ion concentration in seawater (Tables 3 and 4). Cl^- is very stable in the process of fluid migration as well as in many diagenetic reactions; however, its concentration will

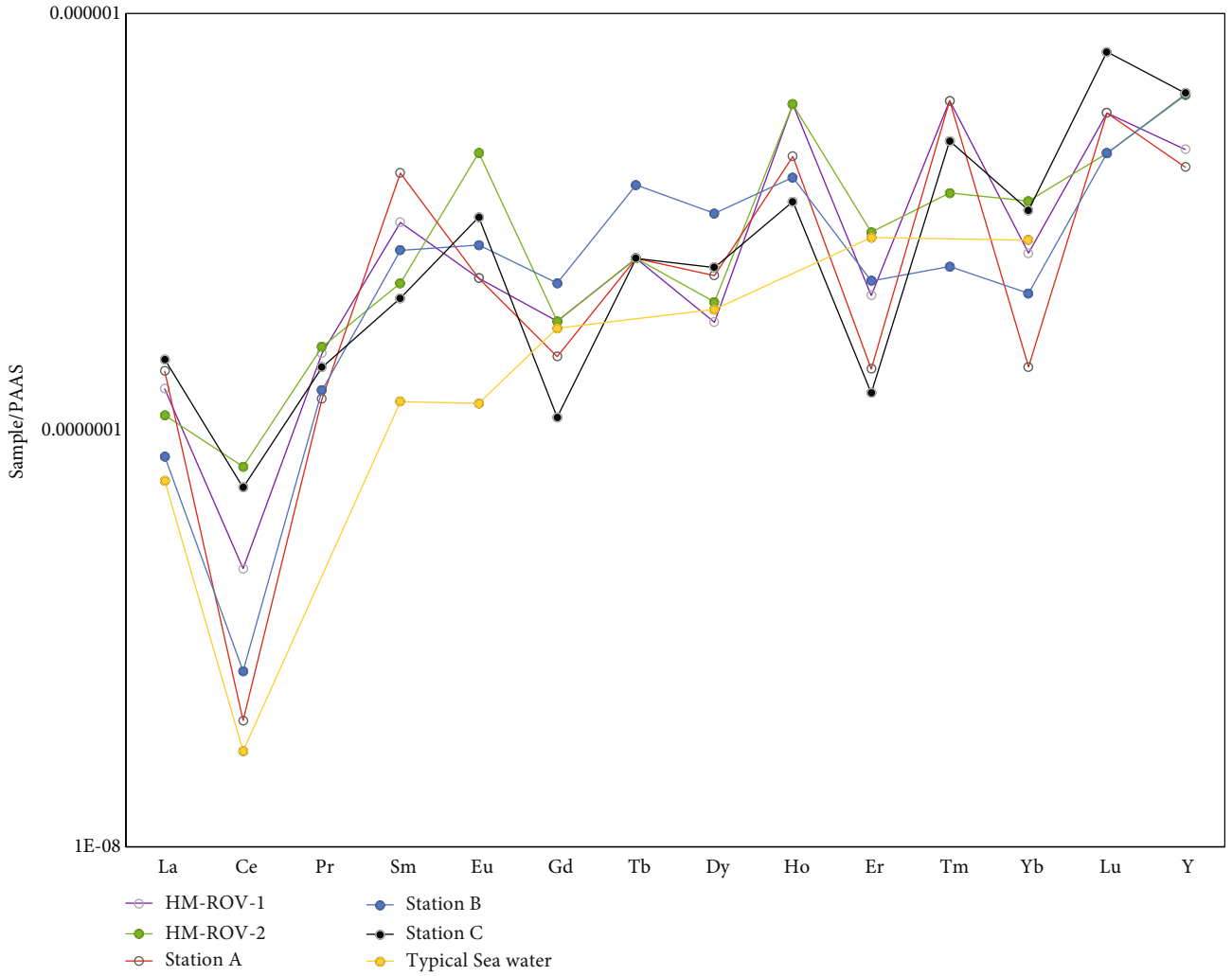

Figure 6: REE distribution curves of water samples at different stations. The PAAS data are from [45]. The REE distribution curves of water samples at all stations show similar general trends, with heavy REE content higher than that for light REEs. The curves were accompanied by an obvious negative Ce anomaly, showing the typical REE distribution curves of seawater.

change when the water volume changes. Thermodynamic reaction processes such as the formation and decomposition of gas hydrate and clay mineral dehydration actually affect the concentration. Therefore, it is helpful to determine the source and sink of the ions in water samples by comparing the ratios of the ions to Cl^-. Although some differences occurred between the ion concentrations in the samples among the stations, the ratios Na^+/Cl^-, K^+/Cl^-, Mg^{2+}/Cl^-, and Ca^{2+}/Cl^- were similar to those in typical seawater (Table 1). In the Na^+-Cl^-, K^+-Cl^-, Mg^{2+}-Cl^-, and Ca^{2+}-Cl^- diagrams, the values in the samples and typical seawater are roughly on the same straight line, showing an obvious positive correlation (Figure 4). Thus, the samples tested are strongly affected by seawater and have similar sources.

5.1.1.1. Differences in Bottom Seawater among Stations A, B, and C. Stations A, B, and C are areas in which cold seeps occur or have previously existed. This study did not detect any cold seep leakages at station A; alternatively, the fluid leakage could have been too weak to support the continued existence of a cold seep ecosystem at that location. A large amount of cold seep leakage related to the decomposition of gas hydrate occurs in the cold seep area in the western QDNB [29]. Therefore, the ion concentration in the cold seep area in this region is lower than the average value of typical seawater, which explains the low ion concentration at station A despite the absence of an active cold seep.

The concentrations of Na^+, Ca^{2+}, Mg^{2+}, Cl^-, and SO_4^{2-} at stations B and C, under the strong influence of cold seep leakage, were significantly lower than those at station A (Tables 3 and 4). Moreover, the ratio SO_4^{2-}/Cl^- at all three stations, ranging from 0.037 to 0.051, was significantly lower than that of typical seawater, at 0.069; $B \approx C < A$ (Tables 3 and 4). Consumption of SO_4^{2-} in the cold seep system includes mainly OSR and AOM. The AOM reaction consumed more SO_4^{2-} as cold seep leakage was obvious at stations B and C. Furthermore, the presence of cold seep ecosystems at stations B and C also increased the amounts of organic substances in these areas. Consequently, more SO_4^{2-} could have been required to produce the OSR reaction, leading to an obvious loss of SO_4^{2-} in the bottom seawater of stations B and C.

Table 3: Main cation concentrations of samples recovered from different cold seeps.

Sample	Ca^{2+} (M/L)	Mg^{2+} (M/L)	K^{+} (M/L)	Na^{+} (M/L)
HM-ROV-1				
PCM-1	0.0046	0.023	0.0052	0.22
PCM-2	0.0045	0.022	0.0053	0.22
PCM-3	0.0040	0.019	0.0048	0.19
PCM-4	0.0039	0.019	0.0048	0.19
Average	0.0042	0.021	0.0050	0.20
HM-ROV-2				
PCM-5	0.0099	0.053	0.010	0.44
PCM-6	0.010	0.053	0.010	0.44
PCM-7	0.0099	0.053	0.010	0.44
PCM-8	0.010	0.053	0.010	0.44
Average	0.0099	0.053	0.010	0.44
Station A				
PCM-9	0.0051	0.024	0.0054	0.26
PCM-10	0.0050	0.024	0.0053	0.26
PCM-11	0.0088	0.044	0.0086	0.41
PCM-12	0.0089	0.045	0.0087	0.42
Average	0.0069	0.034	0.0070	0.34
Station B				
PCM-13	0.0046	0.023	0.0059	0.21
PCM-14	0.0047	0.023	0.0059	0.21
PCM-15	0.0055	0.028	0.0067	0.26
PCM-16	0.0056	0.028	0.0067	0.26
Average	0.0051	0.026	0.0063	0.24
Station B				
PCM-17	0.0047	0.025	0.0057	0.21
PCM-18	0.0049	0.025	0.0058	0.21
PCM-19	0.0048	0.025	0.0058	0.22
PCM-20	0.0047	0.025	0.0057	0.21
°Average	0.0048	0.025	0.0057	0.21

Table 4: Main anion concentrations of samples recovered from different cold seeps.

Sample	Cl^{-} (M/L)	SO_4^{2-} (M/L)
HM-ROV-1		
NCM-1	0.27	0.012
NCM-2	0.27	0.012
NCM-3	0.23	0.010
NCM-4	0.23	0.010
Average	0.26	0.011
HM-ROV-2		
NCM-5	0.58	0.026
NCM-6	0.58	0.027
NCM-7	0.57	0.026
NCM-8	0.57	0.027
Average	0.58	0.026
Station A		
NCM-9	0.31	0.017
NCM-10	0.31	0.016
NCM-11	0.52	0.026
NCM-12	0.52	0.025
Average	0.41	0.021
Station B		
NCM-13	0.27	0.010
NCM-14	0.27	0.0010
NCM-15	0.33	0.012
NCM-16	0.33	0.012
Average	0.30	0.011
Station C		
NCM-17	0.27	0.010
NCM-18	0.27	0.011
NCM-19	0.27	0.011
NCM-20	0.27	0.011
Average	0.27	0.011

Both B/Cl^{-} and Sr/Cl^{-} at stations B and C had significantly large values, indicating that the fluid source was also affected by the mixing of other fluids rich in B and Sr. The concentration of Ba and the ratio Ba/Cl^{-} had high values in our samples. Previous researchers have reported that deep fluid rich in Ba ions is likely to deposit barite on a sulfate–methane interface [49, 50]. However, with the burial of sediments, the previously deposited barite buried downward from the sulfate-deficit zone will be dissolved into Ba ions and transported upward with the cold seep fluid, leading to a higher Ba content in the surface sediments and seawater in the cold seep area.

5.1.1.2. Differences between the Water Samples from HM-ROV-1 and HM-ROV-2. The concentrations of Na^{+}, Ca^{2+}, K^{+}, Mg^{2+}, Cl^{-}, and SO_4^{2-} from the HM-ROV-1 water sample were significantly lower than those from the HM-ROV-2 sample. The concentrations of the former were about half of those of the latter and were close to the bottom seawater values at station C (Tables 3 and 4). The formation of gas hydrate consumes H_2O and creates a high-salinity fluid. Recent studies have proven that many regions of the SCS, including the QDNB, have a high salinity or Cl^{-} concentration resulting from gas hydrate [16, 18, 51, 52]. The increased ion concentrations at HM-ROV-2 might be explained by the presence of high-salinity fluid emitted through gas hydrate formation [9]. However, we cannot rule out the possibility of the value having been affected by the pore water retained in marine sediments, which also has a high salinity.

The reason for the similarity of the concentrations of the main ions, such as Na^{+}, between HM-ROV-1 and station C may be that the sampling position of the bottom seawater at station C was close to HM-ROV-1 and the flow at this vent is larger. Therefore, the bottom seawater at station C is strongly affected by HM-ROV-1. The concentrations of B, Sr, and Ba at HM-ROV-1 were lower than those at HM-ROV-2, whereas B/Cl^{-}, Sr/Cl^{-}, and Ba/Cl^{-} were higher. It is speculated that the fluid flow at HM-ROV-1 is greater than that at HM-ROV-2; thus, the concentrations of B, Sr,

Table 5: Concentrations of REEs and values of δCe and δEu.

Unit	HM-ROV-1 μg/L	HM-ROV-2 μg/L	Station A μg/L	Station B μg/L	Station C μg/L	Typical seawater 10^{-12} mol/kg
La	0.0048	0.0042	0.0053	0.0033	0.0057	20.800
Ce	0.0037	0.0065	0.0016	0.0021	0.0058	9.640
Pr	0.0014	0.0014	0.0011	0.0011	0.0013	—
Sm	0.0018	0.0013	0.0023	0.0015	0.0012	4.320
Eu	0.00025	0.00050	0.00025	0.00030	0.00035	0.823
Gd	0.00085	0.00085	0.00070	0.0011	0.00050	5.200
Tb	0.00020	0.00020	0.00020	0.00030	0.00020	—
Dy	0.00085	0.00095	0.0011	0.0016	0.0012	5.610
Ho	0.00060	0.00060	0.00045	0.00040	0.00035	—
Er	0.00060	0.00085	0.00040	0.00065	0.00035	4.940
Tm	0.00025	0.00015	0.00025	0.00010	0.00020	—
Yb	0.00075	0.0010	0.00040	0.00060	0.00095	4.660
Lu	0.00025	0.00020	0.00025	0.00020	0.00035	—
Y	0.013	0.012	0.012	0.018	0.018	—
δCe	0.33	0.61	0.16	0.25	0.50	—
δEu	0.93	2.3	0.82	1.1	2.1	—

Note: the values of the typical seawater are from [40].

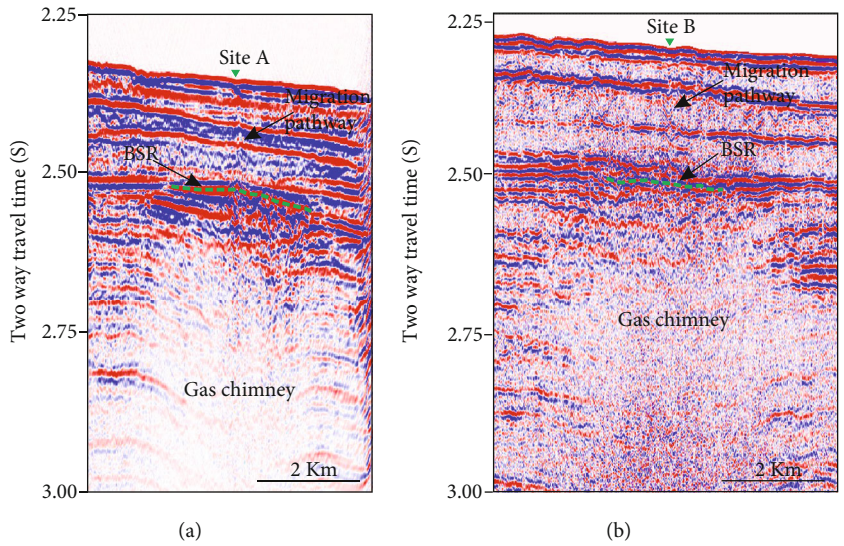

Figure 7: Seismic profiles of stations A and B. (a) Evident gas chimney and a migration pathway blocked by the formation of gas hydrate. (b) Deep gas chimney directly connecting the seafloor with a fluid migration pathway.

and Ba decreased more owing to gas hydrate decomposition. However, the volume of the fluid rich in B, Sr, and Ba at HM-ROV-1 was greater than that at HM-ROV-2. Moreover, the volume of fluid rich in B, Sr, and Ba may be related to intense sediment transformation [46].

Re behaves conservatively in oceans [46, 53, 54] and is influenced by redox environments. The average residence time of Re in the ocean is 7.5×10^5 a. It migrates from seawater under hypoxic conditions and is enriched in reductive marine sediments. Moreover, Re shows different enrichment levels in different hypoxic zones, of these, weak reduction zones are more beneficial than severely hypoxic zones for gathering Re [55]. The Re/Cl^- value of HM-ROV-1 was higher than that of the Pacific Ocean, suggesting the mixing of Re-rich fluids. However, the Re/Cl^- value at HM-ROV-2 was lower than the value in the Pacific Ocean, showing a deficit of Re. One possible reason is that the Re precipitation at HM-ROV-2 was stronger than the input of Re-rich fluids. The flow at HM-ROV-2 is lower than that at HM-ROV-1; thus, the cold seep fluid mixes with the upper layer of seawater less effectively, and the environment at HM-ROV-2 is less open.

5.1.2. Differences in REEs under the Influence of Cold Seep. The REE distribution curves of the water samples at all stations showed a similar general trend, with a higher heavy REE than light REE content. The curves were accompanied by an obvious negative Ce anomaly, showing the typical REE distribution curves of seawater (Figure 6).

The Ce anomaly is related to the oxidation of Ce^{3+} to Ce^{4+}; Ce^{4+} precipitates from the solution in the form of CeO_2 [56, 57]. The bottom seawater of stations A, B, and C showed the same negative Ce anomaly as that in normal seawater (Figure 6). However, the difference in the degree of the Ce anomaly may be related to the relatively reductive environment caused by the active biological reactions and the existence of organic matter in the cold seep, which increased the difficulty of the transformation from Ce^{3+} to Ce^{4+}. The Ce anomalies also affected AOM and alkalinity changes [56, 58–60].

The bottom seawater samples from station C and the vent water samples from HM-ROV-2 showed a slight positive Eu anomaly (Figure 4), which is likely associated with AOM [61, 62]. Recent research has suggested that in a reducing environment, reductive dissolution or desorption of Fe and Mn oxides enables Eu to be released more easily than other REEs; thus, Eu is given priority for entering the liquid and presents a positive Eu anomaly [63]. Moreover, the Eu anomaly is related to the concentration of Ba^{2+} [64].

5.2. Tectonic-Influencing Factors of Cold Seep Formation and Evolution. Comparison of stations A, B, and C revealed that differences in the activity and flow of cold seeps lead to different reflections of their biochemical characteristics, which are often closely related to their regional geology. In recent years, various geophysical techniques such as three-dimensional seismic data have been widely used in the study of cold seeps and their submarine plumbing systems as a powerful tool for examining deep structures [65–67]. In addition, the permeability of migration pathways is believed to be a vital factor in the distribution and temporal and spatial variability of seeps [68]. Therefore, to improve the understanding of the different behaviors of the fluid from cold seep that lead to biochemical differences among cold seeps, we analyzed the seismic profile information of these three stations.

An obvious gas chimney was noted deep in the sampling point of station A; discontinuous parts of a bottom-simulating reflector (BSR) were observed near this depth at ~2.5 s. The reflection masked by gas indicates abundant gas sources in the deep strata. The fluid in the gas chimney was transported upward through the BSR by a nearly vertical migration pathway (Figure 7(a)). However, considering the ROV observations, we found that the migration pathway did not travel straight to the seafloor; rather, the fluid was blocked by the formation of gas hydrate and could not continue to transport upward. We also detected a slight depression on the seafloor in the sampling position, indicating a pockmark, by carefully observing seismic data from station A. The presence of a gas chimney near station A could directly affect the local microgeomorphic characteristics of the corresponding seabed, which could lead to different degrees of local subsidence [69]. This feature combined with the presence of numerous dead clams at station A suggests active paleocold seep leakage at that location.

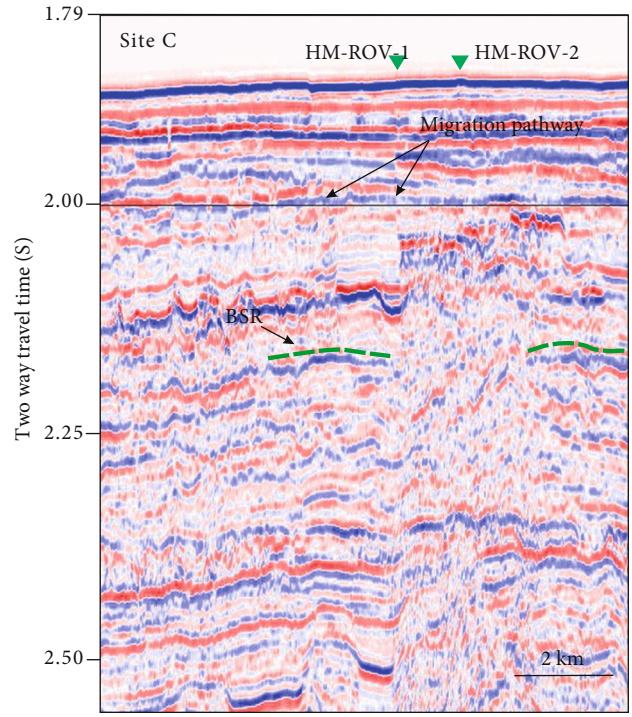

Figure 8: Seismic profile of station C showing the slightly upward slope of the seafloor and the many well-developed migration pathways. The positions of HM-ROV-1 and HM-ROV-2 are shown.

The seismic profile of station B is similar to that of station A, with slight depressions present at the bottom of the seafloor. However, its deep gas chimney directly connects the bottom of the sea with fluid migration pathways, resulting in cold seep leakage at that location (Figure 7(b)). Pockmarks and submarine domes also occur near station B, as do large gas chimneys with sufficient gas sources and cold seep development [69].

The water depth at station C is shallower than that at the other two stations. Owing to abundant gas sources, the seafloor of station C slopes slightly upward. Many well-developed migration pathways and topographies, such as pockmarks and domes, occur in this area. Cold seep activity is very strong here (Figure 8). Topographic uplift is evident at both HM-ROV-1 and HM-ROV-2. According to the ROV observations, small domes have developed near these two cold seep vents. Moreover, geomorphologic features formed by cold seeps such as mud domes have developed near HM-ROV-1. The migration pathways under HM-ROV-1 are more obvious and deeper than those beneath HM-ROV-2; thus, the flow of the cold seep fluid at the former is greater than that at the latter. In addition to the influence of the formation and decomposition of gas hydrate, the source of the cold seep fluid is also likely to be very influenced by the low-salinity groundwater from the sediments deposited during the exchange of sea and land or even from lacustrine sediments in the QDNB, which resulted in the flow of low-salinity fluid from the cold seep. In contrast, the shallower migration pathway below HM-ROV-2 may suggest

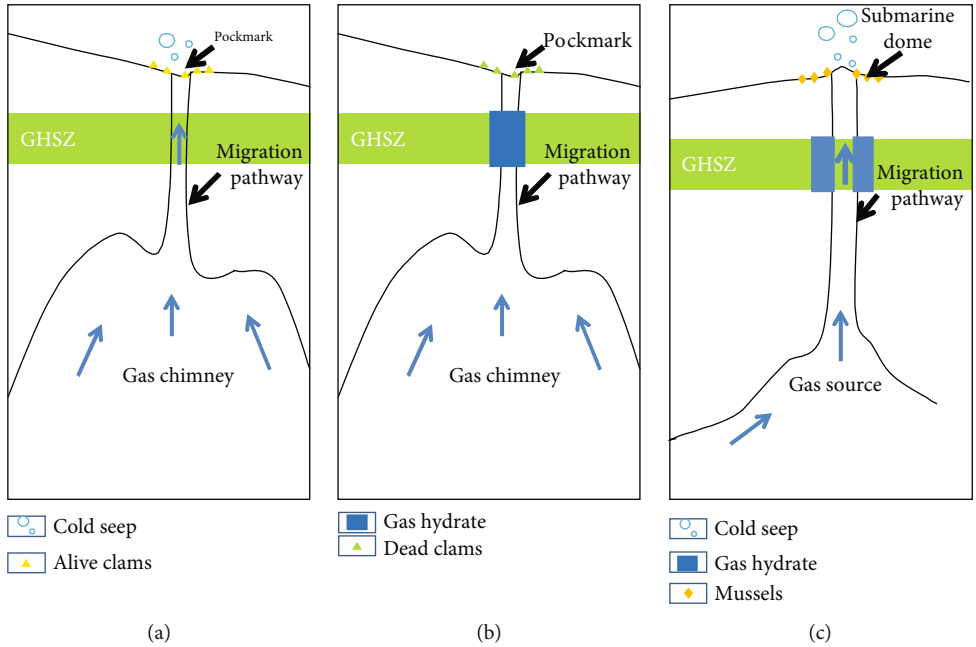

Figure 9: Cold seep evolution in the study area. (a) Fluids from the deep seabed move upward though the fluid migration pathways, generating a cold seep ecosystem with clams as the dominant population and a pockmark on the seafloor. (b) Gas hydrate gradually forms to obstruct the fluid migration pathway, causing the cold seep ecosystem to collapse gradually and kill creatures such as clams. (c) When the flow rate of seepage is sufficiently high, gas hydrates form around the fluid migration pathways instead of inside them due to the strong submarine fluid activity, and a submarine dome and the cold seep ecosystem with mussels as the dominant species are created in this region.

the influence of relatively high-salinity pore water mixing with the marine sediments in the QDNB.

5.3. Cold Seep Formation and Evolution Models in the Study Area. Based on the seismic profiles and information about the bottom seawater chemical anomalies at various stations, we believe that the formation and evolution of cold seeps in this area are closely related to the formation and decomposition of gas hydrate. Many studies have shown that the formation of gas hydrate will reduce the permeability of sediments to different degrees and will change the direction of fluid leakage. For example, one report stated that during the process of fluid migration, gas hydrate will block some of the migration pathways and lead to more concentrated fluid migration in the region [70]. Another study revealed that the lateral migration of methane-containing fluid was driven by the formation of gas hydrate and the blockage of pore space at the seepage center [71]. The seismic profile of station A shows an obvious gas chimney below the sampling point displaying the abundance of gas sources and in-phase axial pull-downs occur in the migration direction, indicating the presence or movement of vulgar fluids, which may result from the upward cold seep fluids. Considering these findings as well as the ROV observations, we consider gas hydrate formation to be the most likely reason for the death of the cold seep at station A.

In addition, many researchers have found that the evolution of ecological communities can reflect changes in cold seep. The type and distribution of cold seep bivalves are influenced by the components, such as methane; the strength of the cold seep fluids; and the bacteria species in the sediments. Mussels inhabit only active cold seep vents with high methane and sulfate contents; they have symbionts and rely on their symbiotic partners to provide most of their nutrients. However, clams have sulfate-reducing bacteria symbionts, which are suitable for cold seep in which the flow rate changes and the spout point is concentrated. Therefore, the presence of mussels and clams can indicate the composition and strength of cold seep fluid [3]. Roberts et al. [72] summarized the responses of hydrocarbons, formation fluids, fluidized sediments, and organisms to different cold seep flow rates.

In this study, the cold seeps at stations A, B, and C displayed the characteristics of inactive cold seeps, cold seep leakage, and active cold seep eruptions, respectively. The differences in their activities and basin spaces were apparent, which could be a good indication of the evolutionary characteristics of the regional cold seeps.

Fluids from the deep seabed move upward though the fluid migration pathways. Initially, the fluid migration pathway is unobstructed, and fluid with a certain flow can reach the seafloor through the stable area of gas hydrate, which is sufficient for supporting the growth and development of clams and other organisms. Therefore, many clams are present, and the cold seep ecosystem is developed. Moreover, the leakage of the cold seep fluid resulted in submarine landforms such as pockmarks (Figure 9(a)) generated near the fluid migration pathway, such as at station B in this study. However, because the upwelling fluid flow rate is insufficient, gas hydrate gradually forms to obstruct the fluid migration

pathway, which decreases the flow capable of reaching the seafloor. Eventually, the fluid flow is unable to continue to provide enough nutrition for its ecological system; thus, the cold seep ecosystem will gradually collapse, and creatures such as clams (Figure 9(b)) will die. Such conditions are similar to those occurring presently at station A.

The study of station C revealed that if the flow rate of seepage is sufficiently high, submarine fluid activity will be strong, leading to abnormal heat conduction and convection and creating temperature changes at various locations. The high flow rate and temperature in the fluid migration pathway will prevent the formation of gas hydrate; thus, the fluid migration pathway will not be easily obstructed, and gas hydrates will form around the fluid migration pathways instead of inside them. Finally, the large flow of fluid will reach the seafloor and spill out in the form of bubbles and plumes (Figure 2(b)) to create submarine landforms such as mud domes and mud volcanoes. Moreover, a unique cold seep ecosystem with mussels as the dominant population will develop in this region (Figure 9(c)). Furthermore, when the fluid flow gradually decreases, this cold seep may gradually change to the states shown in Figures 9(a) and 9(b), and the dominant biological population will also gradually change from mussels to clams.

6. Conclusion

Through the analysis of ROV observations, bottom seawater samples, vent water samples, and seismic profiles obtained from each station, the following conclusions were drawn.

(1) The bottom seawater of the cold seep zone is influenced by seawater and fluid from deep strata. The bottom seawater at stations A, B, and C had lower salinity than typical seawater, and the salinity of the existing stations with cold seep leakage, B and C, was lower than that of station A, which may be related to the decomposition of gas hydrate or the upward migration of groundwater

(2) The chemical characteristics of cold seep fluids are closely related to biochemical reactions such as AOM. The AOM reaction may lead to a loss of SO_4^{2-} in the fluid, leading to S enrichment in the submarine sediments. In addition, the AOM reaction will change the alkalinity of the fluid to reflect a relatively reducible redox environment, which can easily cause anomalies in the amounts of Re, Eu, Ce, and other elements

(3) The cold seep changes are temporal and spatial, which will determine the evolution of the cold seep ecosystem. The formation of gas hydrates may obstruct the fluid migration pathways in the middle flow of the cold seep leakage, causing the cold seep flow to weaken gradually and finally to disappear. In addition, a large flow of cold seep may inhibit gas hydrate formation and cause a large flow of water on the seafloor to be maintained for a longer period. However, the cold seep cannot maintain a state of large flow permanently. In the later stage, as the flow decreases, the cold seep may also gradually weaken and finally disappear

The objectives of this study were to analyze and comprehensively discuss the differences in the ecological community, hydrochemistry, and seismic profiles of different cold seeps by combining several disciplines—including biology, chemistry, and geology—to improve the understanding of the formation and evolution of cold seeps in the study area and the relationship between cold seeps and gas hydrate. However, the tectonic setting of the cold seep area of the western QDNB is extremely complex, with many factors influencing the formation and development of cold seeps. In this study, the research scope and samples were limited and we did not consider differences in the geothermal gradient or the water–rock reaction during the fluid migration. Therefore, the formation and evolution of cold seeps require further research.

Data Availability

The data used to support the findings of this study are available from the corresponding author upon request.

Disclosure

The findings achieved herein are solely the responsibility of the authors.

Conflicts of Interest

The authors declare that they have no conflicts of interest.

Acknowledgments

This work was supported by the National Key R&D Program of China (2018YFC0310000), National Nature Science Foundation of China (Nos. 41776056, 41806071), and the China National Hydrate Project (DD20190217).

References

[1] A. Joseph, "Chapter 6 -Seafloor hot chimneys and cold seeps: mysterious life around them," in *Investigating Seafloors and Oceans*, C. Janco, Ed., pp. 307–375, 2017.

[2] D. Feng and D. Chen, "Authigenic carbonates from an active cold seep of the northern South China Sea: new insights into fluid sources and past seepage activity," *Deep Sea Research Part II: Topical Studies in Oceanography*, vol. 122, pp. 74–83, 2015.

[3] Z. Chen, H. Yang, C. Huang, J. Lu, and W. Yan, "Characteristics of cold seeps and structures of chemoautosynthesis-based communities in seep sediments," *Journal of Tropical Oceanography*, vol. 26, no. 6, pp. 73–82, 2007.

[4] B. Sun, W. Fu, Z. Wang et al., "Characterizing the rheology of methane hydrate slurry in a horizontal water-continuous system," *SPE Journal*, 2019.

[5] W. Fu, Z. Wang, W. Duan, Z. Zhang, J. Zhang, and B. Sun, "Characterizing methane hydrate formation in the non-

Newtonian fluid flowing system," *Fuel*, vol. 253, pp. 474–487, 2019.

[6] W. S. Reeburgh, "Oceanic methane biogeochemistry," *Chemical Reviews*, vol. 107, no. 2, pp. 486–513, 2007.

[7] S. Gong, Y. Peng, H. Bao et al., "Triple sulfur isotope relationships during sulfate-driven anaerobic oxidation of methane," *Earth Planetary Science Letters*, vol. 504, pp. 13–20, 2018.

[8] F. Núñez-Useche, C. Canet, V. Liebetrau et al., "Redox conditions and authigenic mineralization related to cold seeps in Central Guaymas Basin, Gulf of California," *Marine and Petroleum Geology*, vol. 95, pp. 1–15, 2018.

[9] J. Feng, S. Yang, X. Sun, and J. Liang, "Geochemical tracers for methane microleakage activity in the Qiongdongnan Basin," *Journal of Southwest Petroleum University (Science & Technology Edition)*, vol. 40, no. 3, pp. 63–75, 2018.

[10] T. Toki, K. Maegawa, U. Tsunogai, J. Ashi, M. Kinoshita, and T. Gamo, *Distribution of dissolved hydrogen in pore water at cold seep site*, AGU Fall Meeting Abstracts, 2005.

[11] T. Himmler, B. A. Haley, M. E. Torres, G. P. Klinkhammer, G. Bohrmann, and J. Peckmann, "Rare earth element geochemistry in cold-seep pore waters of Hydrate Ridge, northeast Pacific Ocean," *Geo-Marine Letters*, vol. 33, no. 5, pp. 369–379, 2013.

[12] N. Li, D. Feng, L. Chen, H. Wang, and D. Chen, "Using sediment geochemistry to infer temporal variation of methane flux at a cold seep in the South China Sea," *Marine and Petroleum Geology*, vol. 77, pp. 835–845, 2016.

[13] M. Bowles, K. S. Hunter, V. Samarkin, and S. Joye, "Patterns and variability in geochemical signatures and microbial activity within and between diverse cold seep habitats along the lower continental slope, Northern Gulf of Mexico," *Deep Sea Research Part II: Topical Studies in Oceanography*, vol. 129, pp. 31–40, 2016.

[14] X. Wang, N. Li, D. Feng et al., "Using chemical compositions of sediments to constrain methane seepage dynamics: a case study from Haima cold seeps of the South China Sea," *Journal of Asian Earth Sciences*, vol. 168, pp. 137–144, 2018.

[15] T. Yang, S. Jiang, L. Ge et al., "Geochemical characteristics of pore water in shallow sediments from Shenhu area of South China Sea and their significance for gas hydrate occurrence," *Chinese Science Bulletin*, vol. 55, no. 8, pp. 752–760, 2010.

[16] T. Yang, S. Jiang, L. Ge et al., "Geochemistry of pore waters from HQ-1PC of the Qiongdongnan Basin, northern South China Sea, and its implications for gas hydrate exploration," *Science China Earth Sciences*, vol. 56, no. 4, pp. 521–529, 2013.

[17] C. Xu, N. Wu, Z. Sun et al., "Methane seepage inferred from pore water geochemistry in shallow sediments in the western slope of the Mid-Okinawa Trough," *Marine and Petroleum Geology*, vol. 98, pp. 306–315, 2018.

[18] J. Wei, J. Liang, J. Lu, W. Zhang, and Y. He, "Characteristics and dynamics of gas hydrate systems in the northwestern South China Sea - results of the fifth gas hydrate drilling expedition," *Marine and Petroleum Geology*, vol. 110, pp. 287–298, 2019.

[19] F. Scholz, C. Hensen, G. J. De Lange et al., "Lithium isotope geochemistry of marine pore waters - Insights from cold seep fluids," *Geochimica et Cosmochimica Acta*, vol. 74, no. 12, pp. 3459–3475, 2010.

[20] D. Feng, Y. Peng, H. Bao, J. Peckmann, H. H. Roberts, and D. Chen, "A carbonate-based proxy for sulfate-driven anaerobic oxidation of methane," *Geology*, vol. 44, no. 12, pp. 999–1002, 2016.

[21] Y. Hu, M. Luo, L. Chen et al., "Methane source linked to gas hydrate system at hydrate drilling areas of the South China Sea: porewater geochemistry and numerical model constraints," *Journal of Asian Earth Sciences*, vol. 168, pp. 87–95, 2018.

[22] S. Mau, H. Sahling, G. Rehder, E. Suess, P. Linke, and E. Soeding, "Estimates of methane output from mud extrusions at the erosive convergent margin off Costa Rica," *Marine Geology*, vol. 225, no. 1-4, pp. 129–144, 2006.

[23] J. L. Charlou, J. P. Donval, Y. Fouquet et al., "Physical and chemical characterization of gas hydrates and associated methane plumes in the Congo-Angola Basin," *Chemical Geology*, vol. 205, no. 3-4, pp. 405–425, 2004.

[24] E. J. Sauter, S. I. Muyakshin, J.-L. Charlou et al., "Methane discharge from a deep-sea submarine mud volcano into the upper water column by gas hydrate-coated methane bubbles," *Earth and Planetary Science Letters*, vol. 243, no. 3-4, pp. 354–365, 2006.

[25] E. Suess, M. E. Torres, G. Bohrmann et al., "Gas hydrate destabilization: enhanced dewatering, benthic material turnover and large methane plumes at the Cascadia convergent margin," *Earth and Planetary Science Letters*, vol. 170, no. 1-2, pp. 1–15, 1999.

[26] J. C. Sample, "Isotopic evidence from authigenic carbonates for rapid upward fluid flow in accretionary wedges," *Geology*, vol. 24, no. 10, pp. 897–900, 1996.

[27] G. Bohrmann, J. Greinert, E. Suess, and M. Torres, "Authigenic carbonates from the Cascadia subduction zone and their relation to gas hydrate stability," *Geology*, vol. 26, no. 7, pp. 647–650, 1998.

[28] J. C. Sample and M. R. Reid, "Contrasting hydrogeologic regimes along strike-slip and thrust faults in the Oregon convergent margin: evidence from the chemistry of syntectonic carbonate cements and veins," *Geological Society of American Bulletin*, vol. 110, no. 1, pp. 48–59, 1998.

[29] B. Huang, H. Tian, X. Li, Z. Wang, and X. Xiao, "Geochemistry, origin and accumulation of natural gases in the deepwater area of the Qiongdongnan Basin, South China Sea," *Marine and Petroleum Geology*, vol. 72, pp. 254–267, 2016.

[30] H. Guan, D. Birgel, J. Peckmann et al., "Lipid biomarker patterns of authigenic carbonates reveal fluid composition and seepage intensity at Haima cold seeps, South China Sea," *Journal of Asian Earth Sciences*, vol. 168, pp. 163–172, 2018.

[31] D. Feng, J. W. Qiu, Y. Hu et al., "Cold seep systems in the South China Sea: an overview," *Journal of Asian Earth Sciences*, vol. 168, pp. 3–16, 2018.

[32] S. Gong, Y. Hu, N. Li et al., "Environmental controls on sulfur isotopic compositions of sulfide minerals in seep carbonates from the South China Sea," *Journal of Asian Earth Sciences*, vol. 168, pp. 96–105, 2018.

[33] Q. Liang, Y. Hu, D. Feng et al., "Authigenic carbonates from newly discovered active cold seeps on the northwestern slope of the South China Sea: constraints on fluid sources, formation environments, and seepage dynamics," *Deep Sea Research Part I: Oceanographic Research Papers*, vol. 124, pp. 31–41, 2017.

[34] J. Wang, S. Wu, X. Kong et al., "Subsurface fluid flow at an active cold seep area in the Qiongdongnan Basin, northern South China Sea," *Journal of Asian Earth Sciences*, vol. 168, pp. 17–26, 2018.

[35] K. Ru and J. D. Pigott, "Episodic rifting and subsidence in the South China sea," *AAPG Bulletin*, vol. 70, pp. 1136–1155, 1986.

[36] Z. Weilin, "Petroleum geology in deepwater area of northern continental margin in South China Sea," *Acta Petrolei Sinica*, vol. 31, pp. 521–527, 2010.

[37] X. Shi, H. Jiang, J. Yang, X. Yang, and H. Xu, "Models of the rapid post-rift subsidence in the eastern Qiongdongnan Basin, South China Sea: implications for the development of the deep thermal anomaly," *Basin Research*, vol. 29, no. 3, pp. 340–362, 2017.

[38] Q. Sun, S. Wu, G. Yao, and F. Lü, "Characteristics and formation mechanism of polygonal faults in Qiongdongnan Basin, northern South China Sea," *Journal of Earth Science*, vol. 20, no. 1, pp. 180–192, 2009.

[39] X. WANG, S. WU, S. YUAN et al., "Geophysical signatures associated with fluid flow and gas hydrate occurrence in a tectonically quiescent sequence, Qiongdongnan Basin, South China Sea," *Geofluids*, vol. 10, no. 3, 368 pages, 2010.

[40] W. Zhang, J. Liang, X. Yang, P. Su, and Z. Wan, "The formation mechanism of mud diapirs and gas chimneys and their relationship with natural gas hydrates: insights from the deep-water area of Qiongdongnan Basin, northern South China Sea," *International Geology Review*, pp. 1–22, 2018.

[41] T. Lüdmann, H. K. Wong, and P. Wang, "Plio-quaternary sedimentation processes and neotectonics of the northern continental margin of the South China Sea," *Marine Geology*, vol. 172, no. 3-4, pp. 331–358, 2001.

[42] Y. Pin, Z. Di, and L. Zhaoshu, "A crustal structure profile across the northern continental margin of the South China Sea," *Tectonophysics*, vol. 338, no. 1, pp. 1–21, 2001.

[43] I. Rodushkin, C. Paulukat, S. Pontér et al., "Application of double-focusing sector field ICP-MS for determination of ultratrace constituents in samples characterized by complex composition of the matrix," *Science of the Total Environment*, vol. 622-623, pp. 203–213, 2018.

[44] H. Rollison, *Using geochemical data: evalution, presentation, interpretation*, vol. 56, Pearson Education Limited, London, 1993.

[45] S. M. McLennan, "Rare earth elements in sedimentary rocks. Influence of provenance and sedimentary processes," *Reviews in Mineralogy and Geochemistry*, vol. 21, no. 1, pp. 169–200, 1989.

[46] D. Colodner, J. Sachs, G. Ravizza, K. Turekian, J. Edmond, and E. Boyle, "The geochemical cycle of rhenium: a reconnaissance," *Earth and Planetary Science Letters*, vol. 117, no. 1-2, pp. 205–221, 1993.

[47] B. M. Schroot, G. T. Klaver, and R. T. E. Schüttenhelm, "Surface and subsurface expressions of gas seepage to the seabed–examples from the Southern North Sea," *Marine and Petroleum Geology*, vol. 22, no. 4, pp. 499–515, 2005.

[48] L. Vielstädte, J. Karstens, M. Haeckel et al., "Quantification of methane emissions at abandoned gas wells in the Central North Sea," *Marine and Petroleum Geology*, vol. 68, pp. 848–860, 2015.

[49] M. E. Torres, H. J. Brumsack, G. Bohrmann, and K. C. Emeis, "Barite fronts in continental margin sediments: a new look at barium remobilization in the zone of sulfate reduction and formation of heavy barites in diagenetic fronts," *Chemical Geology*, vol. 127, no. 1-3, pp. 125–139, 1996.

[50] M. E. Torres, J. McManus, and C.-A. Huh, "Fluid seepage along the San Clemente Fault scarp: basin-wide impact on barium cycling," *Earth and Planetary Science Letters*, vol. 203, no. 1, pp. 181–194, 2002.

[51] W. U. Lu-shan, Y. A. N. G. Sheng-xiong, L. I. A. N. G. Jinqiang et al., "Geochemical characteristics of sediments at site HQ-48PC in Qiongdongnan area, the north of South China Sea and their implication for gas hydrates," *Geoscience*, vol. 24, no. 3, pp. 534–544, 2010.

[52] P.-C. Chuang, A. W. Dale, K. Wallmann et al., "Relating sulfate and methane dynamics to geology: accretionary prism offshore SW Taiwan," *Geochemistry, Geophysics, Geosystems*, vol. 14, no. 7, pp. 2523–2545, 2013.

[53] M. Koide, V. Hodge, J. S. Yang, and E. D. Goldberg, "Determination of rhenium in marine waters and sediments by graphite furnace atomic absorption spectrometry," *Analytical Chemistry*, vol. 59, no. 14, pp. 1802–1805, 1987.

[54] A. D. Anbar, R. A. Creaser, D. A. Papanastassiou, and G. J. Wasserburg, "Rhenium in seawater: Confirmation of generally conservative behavior," *Geochimica et Cosmochimica Acta*, vol. 56, no. 11, pp. 4099–4103, 1992.

[55] J. L. Morford and S. Emerson, "The geochemistry of redox sensitive trace metals in sediments," *Geochimica et Cosmochimica Acta*, vol. 63, no. 11-12, pp. 1735–1750, 1999.

[56] H. J. W. De Baar, M. P. Bacon, and P. G. Brewer, "Rare-earth distributions with a positive Ce anomaly in the Western North Atlantic Ocean," *Nature*, vol. 301, no. 5898, pp. 324–327, 1983.

[57] C. R. German and H. Elderfield, "Rare earth elements in Saanich Inlet, British Columbia, a seasonally anoxic basin," *Geochimica et Cosmochimca Acta*, vol. 53, no. 10, pp. 2561–2571, 1989.

[58] D. Birgel, D. Feng, H. H. Roberts, and J. Peckmann, "Changing redox conditions at cold seeps as revealed by authigenic carbonates from Alaminos Canyon, northern Gulf of Mexico," *Chemical Geology*, vol. 285, no. 1-4, pp. 82–96, 2011.

[59] A. N. Abbott, B. A. Haley, J. McManus, and C. E. Reimers, "The sedimentary flux of dissolved rare earth elements to the ocean," *Geochimica et Cosmochimica Acta*, vol. 154, pp. 186–200, 2015.

[60] B. Zhu, L. Ge, T. Yang, S. Jiang, and X. Lv, "Stable isotopes and rare earth element compositions of ancient cold seep carbonates from Enza River, northern Apennines (Italy): implications for fluids sources and carbonate chimney growth," *Marine and Petroleum Geology*, vol. 109, pp. 434–448, 2019.

[61] N. D. MacRae, H. W. Nesbitt, and B. I. Kronberg, "Development of a positive Eu anomaly during diagenesis," *Earth and Planetary Science Letters*, vol. 109, no. 3-4, pp. 585–591, 1992.

[62] S. Wang, V. H. Magalhães, L. M. Pinheiro, J. Liu, and W. Yan, "Tracing the composition, fluid source and formation conditions of the methane- derived authigenic carbonates in the Gulf of Cadiz with rare earth elements and stable isotopes," *Marine and Petroleum Geology*, vol. 68, pp. 192–205, 2015.

[63] H. Guo, B. Zhang, Y. Li, L. Wei, and Y. Zhang, "Concentrations and patterns of rare earth elements in high arsenic groundwaters from the Hetao Plain, Inner Mongolia," *Earth Science Frontiers*, vol. 17, no. 6, pp. 59–66, 2010.

[64] L. Carvalho, R. Monteiro, P. Figueira et al., "Rare earth elements in mud volcano sediments from the Gulf of Cadiz, South Iberian Peninsula," *Science of the Total Environment*, vol. 652, pp. 869–879, 2019.

[65] M. Hovland and A. G. Judd, "Seabed pockmarks and seepages: impact on geology," in *Biology and the Marine Environment*, Graham and Trotman, London, 1988.

[66] D. I. Taylor, "Nearshore shallow gas around the U.K. coast," *Continental Shelf Research*, vol. 12, no. 10, pp. 1135–1144, 1992.

[67] S. Garcia-Gil, F. Vilas, and A. Garcia-Garcia, "Shallow gas features in incised-valley fills (Ría de Vigo, NW Spain): a case study," *Continental Shelf Research*, vol. 22, no. 16, pp. 2303–2315, 2002.

[68] A. R. Talukder, "Review of submarine cold seep plumbing systems: leakage to seepage and venting," *Terra Nova*, vol. 24, no. 4, pp. 255–272, 2012.

[69] Q. Feng, J. Tao, Z. Chen, Z. Mu, and M. Weng, "Micro-topographic features detection in natural gas hydrate survey area," *Acta Geoscientica Sinica*, vol. 40, no. 2, pp. 314–318, 2019.

[70] J. Poort, O. M. Khlystov, L. Naudts et al., "Thermal anomalies associated with shallow gas hydrates in the K-2 mud volcano, Lake Baikal," *Geo-Marine Letters*, vol. 32, no. 5-6, pp. 407–417, 2012.

[71] Y. Hu, M. Luo, Q. Liang et al., "Pore fluid compositions and inferred fluid flow patterns at the Haima cold seeps of the South China Sea," *Marine and Petroleum Geology*, vol. 103, pp. 29–40, 2019.

[72] H. H. Roberts, B. A. Hardage, W. W. Shedd, and J. Hunt, "Seafloor reflectivity—an important seismic property for interpreting fluid/gas expulsion geology and the presence of gas hydrate," *The Leading Edge*, vol. 25, no. 5, pp. 620–628, 2006.